Redox-Dependent Metal–Metal Bonding in Trinuclear Metal Chains: Probing the Transition from Covalent Bonding to Exchange Coupling

Mohammed Obies,[a, b] Nicholas R. Perkins,[c] Vaida Arcisauskaite,[a] Graham A. Heath,[d] Alison J. Edwards,[e] and John E. McGrady*[a]

Abstract: The synthesis and physical properties of two new cationic tri-metallic chains, $[(PEt_3)_3RuCl_3M'Cl_3Ru(PEt_3)_3]^{1+}$, M'=Rh and Ir are reported. These are isostructural with a previously reported 17-electron all-ruthenium analogue, but replacing a d^5 Ru^{III} ion in the central position with d^6 Rh^{III}/Ir^{III} has a significant impact on the nature of the metal-metal interactions. All three materials have been characterized electrochemically at the 18-, 17- and 16-electron levels. X-ray crystallography and spectroelectrochemistry, complemented by electronic structure analysis at the DFT and CASPT2 levels, indicate that whilst the presence of a Ru^{III} ion in the center of the chain allows multi-center covalent bonding to develop, a closed-shell Rh^{III}/Ir^{III} ion pushes the system towards the exchange-coupled limit, where the outer Ru centers are only weakly interacting. This family of three isostructural compounds reveals how changes in metal composition can have subtle effects on physical properties of systems that lie close to the localized/delocalized borderline.

Introduction

Arrays of transition metal ions based on face-centered octahedral architectures hold a prominent position in the development of our understanding of the metal-metal bond, largely because the presence of bridging ligands means that the complexes are not wholly dependent on direct overlap of the metal-based orbitals for their integrity. This architecture is therefore able to support a wide range of metal-metal interactions, spanning the entire spectrum from strong covalent bonding, as for example in $[Ru_2Cl_9]^{3-}$ and $[W_2Cl_9]^{3-}$, to the weak antiferromagnetic coupling in $[Cr_2Cl_9]^{3-}$.[1] The balance between these two limits can be understood in a Hubbard-type framework as a compromise between the orbital overlap, which favors delocalization and hence covalent bonding, and electron-electron repulsions which tend to favor localization and hence antiferromagnetic coupling. In a small number of cases the balance between these factors is extremely delicate: an example is the $(Cp*RuCl)_2(\mu-Cl)_2$ dimer where distinct isomers corresponding to the covalently bonded (Ru–Ru = 2.930(1) Å) and exchange-coupled (Ru–Ru = 3.752(1) Å) limits are isolated in the same crystal.[2] Given the importance of the electron-electron repulsion term in determining the degree of delocalization, it comes as no surprise that the description of metal-metal bonds in these bridged systems represents a substantial challenge to theory. Hoffmann and co-workers set out the symmetry-related aspects of the problem using extended Hückel theory,[3] but subsequent studies using density functional theory have revealed just how sensitive the problem is to the choice of exchange functional. In particular, the inclusion of exact Hartree–Fock exchange in hybrid functionals such as B3LYP tends to favor localized electron density distributions and hence antiferromagnetic coupling over covalent bonding.[4] More recently, multi-configurational SCF (CASSCF) approaches have been applied to the problem, revealing the importance of a correct treatment of the multi-configurational nature of the problem.[5] Much of the early work in this field focused on clusters containing only two transition metal centers, but careful synthetic work has extended the chemistry of face-shared octahedral chains to trimetallic systems.[6–11] The first fully characterized trinuclear complex based on the face-sharing architecture was $[Ru_3Cl_{12}]^{4-}$, with a 16-electron ($[Ru_3]^{8+}$) core and a Ru–Ru bond length of 2.805(1) Å.[6] In an early application of the SCF-Xα-SW methodology, Bursten and Cotton

[a] M. Obies, Dr. V. Arcisauskaite, Prof. Dr. J. E. McGrady
Department of Chemistry, University of Oxford,
South Parks Road, Oxford, OX1 3QZ (UK)
E-mail: john.mcgrady@chem.ox.ac.uk

[b] M. Obies
College of Pharmacy, University of Babylon
Hilla (Iraq)

[c] Dr. N. R. Perkins
Research School of Chemistry, The Australian National University
Canberra, ACT0200 (Australia)

[d] Prof. Dr. G. A. Heath
Physical, Engineering and Mathematical Sciences, ADFA
Northcott Road, Canberra, ACT2600 (Australia)

[e] Dr. A. J. Edwards
Australian Centre for Neutron Scattering
Australian Nuclear Science and Technology OrganisationNew Illawarra
Road, Lucas Heights, NSW 2232 (Australia)
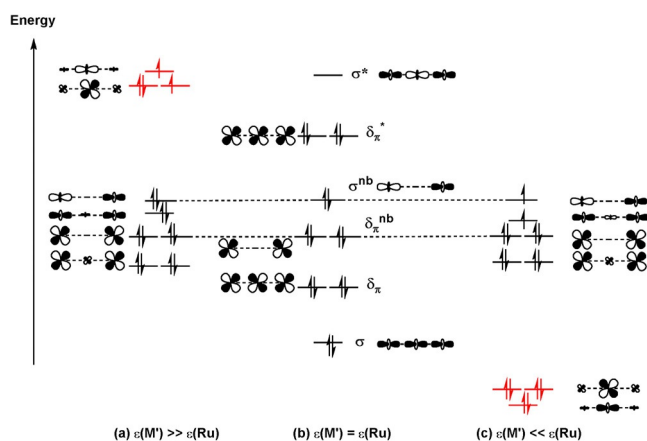
Scheme 1. Three limiting perspectives on the metal-metal bonding in a 16-electron tri-metallic chain, RuM′Ru, in a face-shared octahedral architecture (D_{3d} symmetry): (a) the orbitals on the central metal are higher in energy than those on the outer metals (b) all three metals have similar orbital energies, and (c) the orbitals on the central metal are lower than the outer metals. Orbitals localized on the central metal are highlighted in red.

showed that the nine orbitals of the octahedral t_{2g} sets generate linear combinations with local σ (σ, σ^{nb}, and σ^{*}) and mixed δ/π symmetry (δ_{π}, δ_{π}^{nb}, and δ_{π}^{*}), Scheme 1(b). Populating this array with 16 valence electrons leaves only the σ^{*} orbital vacant, giving a net Ru—Ru bond order of $^{1}/_{2}$,[12] consistent with the rather longer Ru—Ru bond length in $[Ru_3Cl_{12}]^{4-}$ compared to 2.725(3) Å in $[Ru_2Cl_9]^{3-}$, where the bond order is 1.0.[13] Cotton and Torralba have subsequently extended the scope of ruthenium chemistry based on this architecture through the isolation of the two phosphine complexes $(PR_3)_2ClRuCl_3RuCl_3RuCl(PR_3)_2$ (R = Et, tBu), both of which also have a $[Ru_3]^{8+}$ core and Ru—Ru bond lengths of ≈ 2.8 Å. One-electron oxidation of these compounds removes a weakly antibonding δ_{π}^{*} electron, with only minor structural consequences. Cotton and Torralba also described the structure of the 17-electron $[Ru_3]^{7+}$ system, $[(PEt_3)_3RuCl_3RuCl_3Ru(PEt_3)_3]^{1+}$,[14–16] while Kölle and co-workers reported an 18-electron $[Ru_3]^{6+}$ analogue, (p-cymene)RuCl_3RuCl_3Ru(p-cymene).[17] The Ru—Ru separations of 3.083(1) Å and 3.1975(8) Å, respectively, in these latter two systems are consistent with net Ru—Ru bond orders of $^{1}/_{4}$ and 0. The $[Ru_3]$ core therefore appears to be very tolerant to a wide range of oxidation states, from 18-electron $Ru^{II}Ru^{II}Ru^{II}$ to 15-electron $Ru^{III}Ru^{III}Ru^{III}$ through all points in between, and the changing structure of the Ru_3 unit reflects the increasing covalent Ru-Ru bond order.

In a number of recent papers, we have explored the transition from covalent metal–metal bonding to antiferromagnetic coupling in molecular systems.[18] This transition can be approached, in the context of Scheme 1, by considering the impact of changing the identity of the central metal ion of the linear array. At one extreme, if the orbitals of the central metal (shown in red) are very high in energy, the orbitals on the terminal metal become doubly occupied (Scheme 1 (a)) and the L_3RuCl_3 units act simply as tripodal ligands. At the opposite limit, if the orbitals on the central metal are much more stable than those on the terminal sites, it is the central MCl_6 unit that

becomes diamagnetic and acts as a bridging ligand connecting two paramagnetic Ru^{III} centers. The situation described by Cotton and Bursten for $[Ru_3Cl_{12}]^{4-}$, where the d orbitals on all three metals have similar energies, lies somewhere between these two limits, and in such circumstances, covalent bonding emerges.[12] In this paper, we explore the transition from covalent to exchange-coupled regimes in the trinuclear series by comparing the 17-electron $[(PEt_3)_3RuCl_3RuCl_3Ru(PEt_3)_3]^{1+}$ cation (1^{1+}) with its isostructural Rh and Ir analogues, $[(PEt_3)_3RuCl_3RhCl_3Ru(PEt_3)_3]^{1+}$ (2^{1+}) and $[(PEt_3)_3RuCl_3IrCl_3Ru(PEt_3)_3]^{1+}$ (3^{1+}), structures of which we report for the first time. 2^{1+} and 3^{1+} are isolated at the 18-electron level, but spectroelectrochemistry allows both systems, along with the ruthenium analogue, to be accessed and characterized at common 17- and 16-electron levels. In the context of Scheme 1, we note that the reduction potentials of the isolated $[MCl_6]^{2-}$ complexes (all in V vs. Ag/AgCl) are: $Ru^{III/II}$ −1.53; $Ru^{IV/III}$ −0.05; $Rh^{IV/III}$ +0.72; $Ir^{IV/III}$ −0.02.[19] The similarity of the $Ru^{IV/III}$ and $Ir^{IV/III}$ couples highlights the diagonal relationship between the elements. We anticipate that the much higher potential in the case of Rh should cause a very distinct shift towards the scenario depicted in Scheme 1(c). We first report the synthesis, structure, electrochemical, and spectroelectrochemical properties of 2^{1+} and 3^{1+} and compare them to a sample of 1^{1+} prepared following the protocol set out by Cotton and Torralba.[16] We then compare and contrast the electronic structures of the Ru, Rh, and Ir systems at various oxidation levels using both density functional theory and multi-configurational self-consistent field (MCSCF) methods (CASPT2). Our results suggest that the switch from Ru to Rh in the central position does indeed induce a shift from a delocalized regime to one that is more characteristic of super-exchange.

Results and Discussion

X-ray studies of $[(PEt_3)_3RuCl_3RhCl_3Ru(PEt_3)_3](CF_3SO_3)$ (2) and $[(PEt_3)_3RuCl_3IrCl_3Ru(PEt_3)_3](CF_3SO_3)$ (3)

The structures of the cationic components of **2** and **3** are shown in Figure 1, which highlights the face-shared bi-octahedral architecture. A full list of bond lengths and angles is given in the supporting information (Table S1). The Rh—Ru and Ir—Ru separations of 3.1690(3) and 3.2332(3) Å, in 2^{1+} and 3^{1+}, respectively, are longer than the Ru—Ru distance of 3.083(1) Å in Cotton's 17-electron $[(PEt_3)_3RuCl_3RuCl_3Ru(PEt_3)_3]^{1+}$, but similar to the value of 3.1975(8) Å in Kölle's 18-electron (p-cymene)RuCl_3RuCl_3Ru(p-cymene). The metal-ligand bond lengths and angles are otherwise very similar in **2** and **3** (see Supporting Information), small differences being attributable to the slightly larger radius of Ir compared to Rh.

Electrochemistry

The measured electrode potentials (vs. Ag/AgCl) for compounds **1**, **2**, and **3** are collected in Table 1. For compound **1**, the reduction wave at −0.14 V can be safely assigned to a
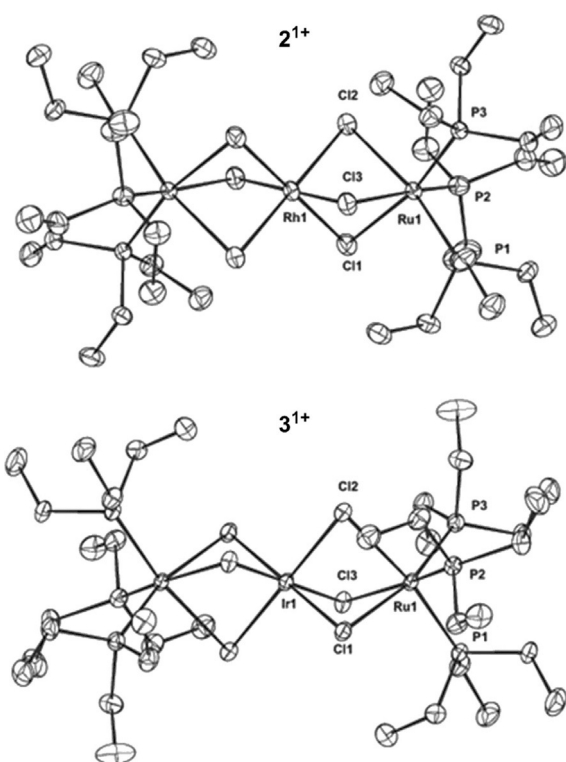
Figure 1. Displacement ellipsoid plot (50% probability) for the cations, [(PEt$_3$)$_3$RuCl$_3$RhCl$_3$Ru(PEt$_3$)$_3$]$^{1+}$ (**2**$^{1+}$) and [(PEt$_3$)$_3$RuCl$_3$IrCl$_3$Ru(PEt$_3$)$_3$]$^{1+}$ (**3**$^{1+}$).

Table 1. Oxidation and reduction potentials for **1**, **2**, and **3** (all examined in the 1+ state) vs. Ag/AgCl. (Fc/Fc$^+$ occurs at 0.55 V).

	$E_{1/2}$ (red) [V]	$E_{1/2}$ (ox1) [V]	$E_{1/2}$ (ox2) [V]
1 (M=Ru)	−0.14	+1.08	+1.78
2 (M=Rh)		+1.45	+1.62
3 (M=Ir)		+1.34	+1.67

Ru$^{II/III}$ couple, the stabilization of 1.39 V relative to [RuCl$_6$]$^{2-/3-}$ being due to the presence of two dicationic Ru(PEt$_3$)$_3$ caps. For compounds **2** and **3**, the absence of a reduction wave is entirely consistent with the formulation of the monocations as 18-electron, closed shell molecules; the only plausible assignment of oxidation states for these species is Ru^{II}(Rh/Ir)^{III}Ru^{II}. One- and two-electron oxidation processes could, in principle, involve redox events at either the central metal or the terminal ruthenium centers, although the high potential of the Rh$^{IV/III}$ couple[19] in [RhCl$_6$]$^{2-/3-}$ suggests that the former is unlikely in **2**. Consistent with this proposal, we note that the mean of the two oxidation waves of 1.53 V in **2** is only slightly more positive than the value of 1.40 eV for bimetallic [(PEt$_3$)$_3$RuCl$_3$Ru(PEt$_3$)$_3$]$^{1+}$, where the redox events are unambiguously Ru$^{II/III}$ couples.[20] The smaller separation between the two oxidation waves in **2** (0.17 V) compared to [(PEt$_3$)$_3$RuCl$_3$Ru(PEt$_3$)$_3$]$^{1+}$ (0.62 V) reflects the increased separation between the redox-active centers, and hence the reduced capacity for stabilization due to ion-pairing in the larger trimetallic cations.[21] The average of the two oxidation waves for **3**

is also very similar at 1.51 V, but the somewhat lower value for $E_{1/2}$(ox1) suggests a greater participation of Ir in the frontier orbitals.

The assignment of oxidation states is less obvious in 17-electron **1**$^{1+}$, where all three metals are identical. Given that the central Ru is surrounded by six π-donor chloride ligands, a formulation as Ru^{II}Ru^{III}Ru^{II} seems most realistic, placing the unpaired electron on the central metal and not on the terminal pair, as in isoelectronic **2/3**$^{2+}$. This then leaves the 16-electron dication, **1**$^{2+}$, to be formulated as Ru^{II}Ru^{III}Ru^{III}↔Ru^{III}Ru^{III}Ru^{II}, although the Ru^{II}Ru^{IV}Ru^{II} alternative cannot be excluded given the different coordination environments of the central and terminal sites. In any case, the presence of a discrete reduction wave in **1**, 1.22 V negative of the first oxidation wave, reflects a qualitatively different frontier orbital arrangement from the isovalent Rh and Ir species. We return to this discussion in the following section on Electronic structure analysis.

Spectroelectrochemistry

The UV/Visible spectra of the mono-, di-, and trications of the iridium compound, **3**$^{1+/2+/3+}$ and the mono- and dication of the ruthenium analogue, **1**$^{1+/2+}$, measured in situ in an OTTLE cell, are shown in Figure 2. The spectra are arranged to facilitate comparisons between isoelectronic pairs. The spectrum of 18-electron **2**$^+$ is featureless below 20000 cm^{-1}, as would be expected for a system with a closed d^{6}d^{6}d^6 valence shell. At the 17-electron level, the spectra of both systems are much richer. **1**$^{1+}$ has a narrow and relatively intense band at 11340 cm^{-1} ($\varepsilon = 5920$ dm^{3}mol^{-1}cm^{-1}) a feature that is highly characteristic of σ→σ* transitions in related systems. In the classic ruthenium "blue", [Ru$_2$Cl$_3$(NH$_3$)$_6$]$^{2+}$, for example, a feature assigned to the σ→σ* transition is located at ≈17000 cm^{-1},[22] whereas in [Ru$_2$Cl$_9$]$^{4-}$ and [Ru$_2$Cl$_3$(PMe$_3$)$_6$]$^{2+}$, the corresponding transitions are found at 12400 cm^{-1} and 9350 cm^{-1}, respectively.[20,23] In all these 11-electron systems the σ→σ* absorption band provides a direct measure of the separation of the one-electron orbitals. Several bands with lower intensity are apparent in the near-IR region for **3**$^{2+}$, with the most intense appearing well below 10000 cm^{-1} (5730 cm^{-1}, $\varepsilon = 3070$ dm^{3}mol^{-1}cm^{-1}). Qualitatively, this suggests a somewhat weaker metal-metal interaction in **3**$^{2+}$ versus **1**$^{1+}$.

The differences between **1** and **3** are most pronounced at the 16-electron level, where **1**$^{2+}$ shows a very intense peak at 9950 cm^{-1} ($\varepsilon = 10860$ dm^{3}mol^{-1} cm^{-1}). Although UV/Vis spectra were not reported for Cotton's (PR$_3$)$_2$ClRuCl$_3$RuCl(PR$_3$)$_2$ complexes (isoelectronic with **1**$^{2+}$), their green color is consistent with a strong absorption in the same region. The corresponding region in 16-electron **2**$^{3+}$ features a less intense band at lower frequency (8000 cm^{-1}).

Electronic structure analysis

In the following sections, we compare and contrast the electronic structure of the all-ruthenium chain, **1**, with its rhodium and iridium analogues, **2** and **3**. Specifically, we focus on com-
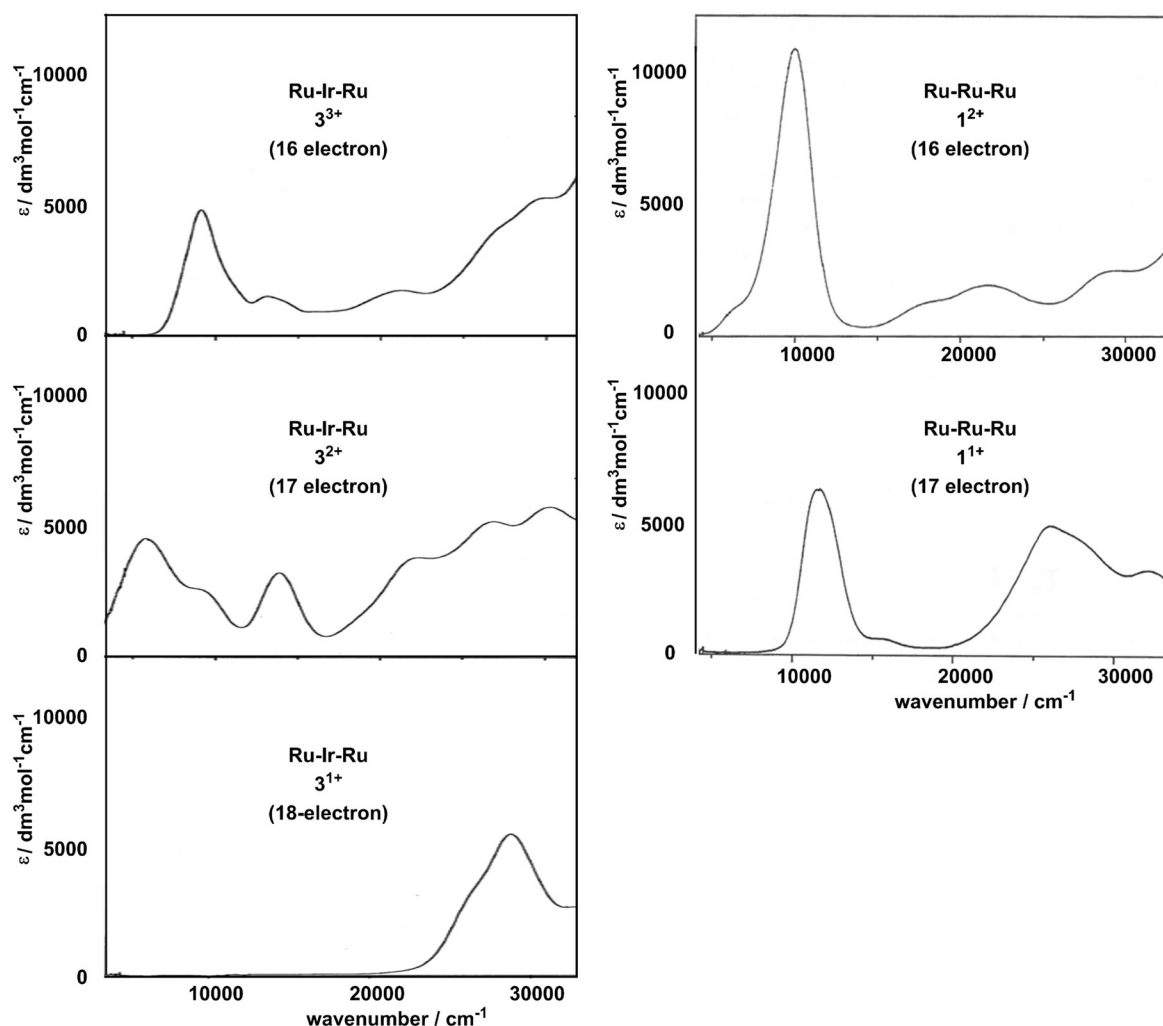
Figure 2. Near-IR/UV spectra of [(PEt$_3$)$_3$RuCl$_3$IrCl$_3$Ru(PEt$_3$)$_3$]$^{1+/2+/3+}$ (**3**$^{1+/2+/3+}$) and [(PEt$_3$)$_3$RuCl$_3$RuCl$_3$Ru(PEt$_3$)$_3$]$^{1+/2+}$ (**1**$^{1+/2+}$).

parisons between pairs with identical electron counts, **1**$^{1+}$ versus **2/3**$^{2+}$ (17 valence electrons), and **1**$^{2+}$ versus **2/3**$^{3+}$ (16 valence electrons). Our aim is to establish how a change in the central metal of the chain influences the nature of the metal–metal bonding. We choose two quite distinct functionals, BLYP and its hybrid with 20% Hartree–Fock exchange, B3LYP, because previous studies have shown that these offer rather different pictures of metal-metal bonds.[18c] The high symmetry of the P$_3$RuCl$_3$RuCl$_3$RuP$_3$ core (D_{3d}) is, in principle, a powerful tool to simplify the analysis of the electronic structure, as it imposes a clean separation between the σ and δ$_\pi$ symmetry interactions in Scheme 1. However the Et substituents on the phosphines interlock in the crystal structures in order to reduce steric repulsions, and it is not possible to impose D_{3d} symmetry without introducing unreasonable steric clashes. We have, therefore, chosen to tackle the problem in two stages. First, geometries of **1**$^{1+}$, **2**$^{1+}$, and **3**$^{1+}$ are optimized without any imposed symmetry, using PMe$_3$ as a model for the full PEt$_3$ ligand: this minor simplification alleviates the problem of facile rotation about the C–C bonds but still captures the majority of the inductive and steric effects of the alkyl groups. With the ability of the computational model to reproduce the key ex-

perimental observables (i.e., the X-ray data) established, we then present a detailed analysis of the various D_{3d}-symmetric electronic states using the highly simplified model ligand PH$_3$. Whilst this is clearly a much grosser simplification, comparison with the PMe$_3$ case suggests that the electronic structure description is not compromised to any great extent. Throughout the text, we use a prime (′) to distinguish the model systems with PH$_3$ from the real systems: **1**$^{′1+}$ for [(PH$_3$)$_3$RuCl$_3$RuCl$_3$Ru(PH$_3$)$_3$]$^{1+}$ versus **1**$^{1+}$ for [(PEt$_3$)$_3$RuCl$_3$RuCl$_3$Ru(PEt$_3$)$_3$]$^{1+}$.

Optimized structures of [(PMe$_3$)$_3$RuCl$_3$MCl$_3$Ru(PMe$_3$)$_3$]$^{1+}$

The optimized structural parameters of [(PMe$_3$)$_3$RuCl$_3$MCl$_3$Ru(PMe$_3$)$_3$]$^{1+}$, M=Ru, Rh, and Ir, are collected in Table 2, where they are compared to the available crystallographic data for **1**$^{1+}$, **2**$^{1+}$, and **3**$^{1+}$. The correspondence is in general encouraging, with the Ru–Ru separation of 3.083(1) Å in **1**$^{1+}$ reproduced to within 0.02 Å using either the BLYP or B3LYP functional. Ru–M distances for **2**$^{1+}$ and **3**$^{1+}$ are slightly less accurate, perhaps reflecting the fact that there is no direct M–Ru bonding in these 18-electron systems, as a result of

Table 2. Comparison of the optimized structural parameters of $[(PMe_3)_3RuCl_3MCl_3Ru(PMe_3)_3]^{1+}$ with crystallographic data for $\mathbf{1}^{1+}$ (M = Ru), $\mathbf{2}^{1+}$ (M = Rh) and $\mathbf{3}^{1+}$ (M = Ir) (distances in Å).

		Ru–M	Ru–Cl	Ru–P	M–Cl	ρ(Ru)	ρ(M)
$\mathbf{1}^{1+}$	BLYP	3.10	2.57	2.29	2.42	0.11	0.68
	B3LYP	3.09	2.56	2.30	2.41	0.06	0.79
	X-ray[16]	3.083(1)	2.50	2.31	2.36		
$\mathbf{2}^{1+}$	BLYP	3.23	2.58	2.28	2.40		
	B3LYP	3.19	2.56	2.29	2.39		
	X-ray	3.1690(3)	2.52	2.29	2.34		
$\mathbf{3}^{1+}$	BLYP	3.27	2.59	2.28	2.41		
	B3LYP	3.22	2.57	2.28	2.40		
	X-ray	3.2332(3)	2.54	2.29	2.35		

which the potential energy surface is very flat. Nevertheless, the agreement between experiment and theory is sufficiently good to indicate that the chosen computational model is acceptable.

D_{3d}–symmetrized systems with the model PH_3 ligand, $[(PH_3)_3RuCl_3MCl_3Ru(PH_3)_3]^{z+}$

17-Electron systems: Relative energies, optimized bond lengths and Mulliken spin densities for the various electronic states of 17-electron $\mathbf{1'}^{1+}$, $\mathbf{2'}^{2+}$, and $\mathbf{3'}^{2+}$ are collected in Table 3 (upper section), using both the BLYP and B3LYP functionals. In the all-ruthenium chain, $\mathbf{1'}^{1+}$, the ground state has $^2A_{1g}$ symmetry with an optimized Ru–Ru separation of 3.13 Å compared to a value of 3.10 Å for the $[(PMe_3)_3RuCl_3MCl_3Ru(PMe_3)_3]^{1+}$ model and 3.083(1) Å for $\mathbf{1}^{1+}$ itself. The Mulliken spin densities of the $^2A_{1g}$ state are also very

similar to those of the (unsymmetrized) system with the full PMe_3 ligands, and the Kohn–Sham orbitals summarized in Figure 3 confirm that the SOMO has σ* character, as anticipated in Scheme 1. A dipole-allowed $^2A_{1g} \rightarrow {}^2A_{2u}$ excitation (σ$^{nb} \rightarrow$ σ*) is predicted at 11 500 cm^{-1} (TD-DFT, BLYP), almost coincident with the intense absorption at 11 340 cm^{-1} in the spectrum of $\mathbf{1}^{1+}$ (Figure 2), offering further support for the assignment of a $^2A_{1g}$ ground state. The close correspondence between the structural parameters in Tables 2 and 3 suggests that the progressive simplification of the phosphine ligands does not compromise the description of the metal-metal bonding to any great extent. The Mulliken spin densities of 0.73 and 0.09 (BLYP) on the central and outer ruthenium centers in the $^2A_{1g}$ state approach the limiting values of 1.0 and 0.0 anticipated for a $Ru^{II}Ru^{III}Ru^{II}$ ($d^6d^5d^6$) oxidation state pattern. In the heterometallic 17-electron analogues, $\mathbf{2'}^{2+}$ and $\mathbf{3'}^{2+}$, the ground state is again predicted to have $^2A_{1g}$ symmetry, with Ru–M separations of ≈3.10 Å, only marginally shorter than those in $\mathbf{1'}^{1+}$. However, the Mulliken spin densities of 0.30 and 0.33 on Rh and Ru, respectively, reveal a rather different picture, with the unpaired electron delocalized much more evenly over all three metal centers. To put these values in context, the limit where all three Rh t_{2g} orbitals become fully occupied (as in Scheme 1 (c)), would generate a $Ru^{II}Rh^{III}Ru^{II} \leftrightarrow Ru^{III}Rh^{III}Ru^{II}$ oxidation state pattern ($d^{5.5}d^6d^{5.5}$) with spin densities of 0 and 0.5 on Rh and Ru, respectively. The computed values of 0.30 and 0.33 in $\mathbf{2'}^{2+}$ are thus intermediate between the two extreme limiting formulations defined by Schemes 1 (a) and (c). The more readily oxidized Ir center in $\mathbf{3'}^{2+}$ pushes the Mulliken spin densities back towards the $d^6d^5d^6$ limit (0.38/0.27).

Table 3. Relative energies, optimized bond lengths, and Mulliken spin densities of the key states of model 17- and 16-electron systems, $[(PH_3)_3RuCl_3MCl_3Ru(PH_3)_3]^{z+}$.

17-Electron systems		$\mathbf{1'}^{1+}$, [RuRuRu]$^+$				$\mathbf{2'}^{2+}$, [RuRhRu]$^{2+}$				$\mathbf{3'}^{2+}$, [RuIrRu]$^{2+}$			
		E(rel) [eV]	M–M [Å]	ρ(Ru$_i$)	ρ(Ru$_o$)	E(rel) [eV]	M–M [Å]	ρ(Rh$_i$)	ρ(Ru$_o$)	E(rel) [eV]	M–M [Å]	ρ(Ir$_i$)	ρ(Ru$_o$)
BLYP	$^2A_{1g}$	0.00	3.13	0.73	0.09	0.00	3.09	0.30	0.33	0.00	3.10	0.38	0.27
	$^2E_{1g}$	+0.14	3.26	0.78	0.03	+0.04	3.25	0.30	0.26	+0.07	3.29	0.31	0.20
	$^2A_{2u}$	+1.44	3.22	−0.03	0.42	+0.25	3.21	−0.01	0.44	+0.49	3.25	−0.01	0.46
B3LYP	$^2A_{1g}$	0.00	3.10	0.83	0.04	0.00	3.02	0.29	0.32	0.00	3.04	0.42	0.23
	$^2E_{1g}$	+0.64	3.22	0.81	0.02	+0.35	3.19	0.13	0.30	+0.44	3.24	0.31	0.19
	$^2A_{2u}$	+1.73	3.15	−0.04	0.40	+0.18	3.16	−0.03	0.45	+0.53	3.19	−0.02	0.46
16-Electron systems		$\mathbf{1'}^{2+}$, [RuRuRu]$^{2+}$				$\mathbf{2'}^{3+}$, [RuRhRu]$^{3+}$				$\mathbf{3'}^{3+}$, [RuIrRu]$^{3+}$			
		E(rel) [eV]	M–M [Å]	ρ(Ru$_i$)	ρ(Ru$_o$)	E(rel) [eV]	M–M [Å]	ρ(Rh$_i$)	ρ(Ru$_o$)	E(rel) [eV]	M–M [Å]	ρ(Ir$_i$)	ρ(Ru$_o$)
BLYP	$1\,^1A_{1g}$	+0.05	2.92	0.00	0.00	+0.24	2.94	0.00	0.00	+0.07	2.93	0.00	0.00
	BS(σσ)	''	''	''	''	+0.12	3.04	0.00	±0.72	+0.07	2.95	0.00	±0.26
	$^3A_{2u}$	+0.67	3.10	0.69	0.52	+0.14	3.09	0.26	0.78	+0.25	3.11	0.36	0.72
	$1\,^3A_{2g}$	+0.13	3.28	1.14	0.18	0.00	3.26	0.29	0.60	0.00	3.30	0.43	0.51
	$1\,^3E_{1g}$	0.00	3.12	1.14	0.25	+0.04	3.12	0.38	0.65	+0.03	3.14	0.50	0.57
	$1\,^3E_{1u}$	+0.72	3.11	0.73	0.50	+0.21	3.09	0.30	0.75	+0.29	3.10	0.39	0.69
B3LYP	$1\,^1A_{1g}$	0.00	2.87	0.00	0.00	+0.88	2.87	0.00	0.00	+0.39	2.87	0.00	0.00
	BS(σσ)	''	''	''	''	+0.01	3.09	0.00	±0.94	0.00	3.02	0.00	±0.80
	$^3A_{2u}$	+0.38	3.03	0.64	0.54	0.00	3.09	0.08	0.93	+0.02	3.07	0.20	0.84
	$1\,^3A_{2g}$	+0.01	3.25	1.43	0.08	+0.67	3.20	0.20	0.66	+0.48	3.25	0.43	0.51
	$1\,^3E_{1g}$	+0.31	3.10	1.23	0.19	+0.98	3.05	0.33	0.67	+0.72	3.07	0.51	0.55
	$1\,^3E_{1u}$	+0.93	3.09	0.83	0.47	+1.13	3.03	0.30	0.74	+0.94	3.06	0.46	0.66
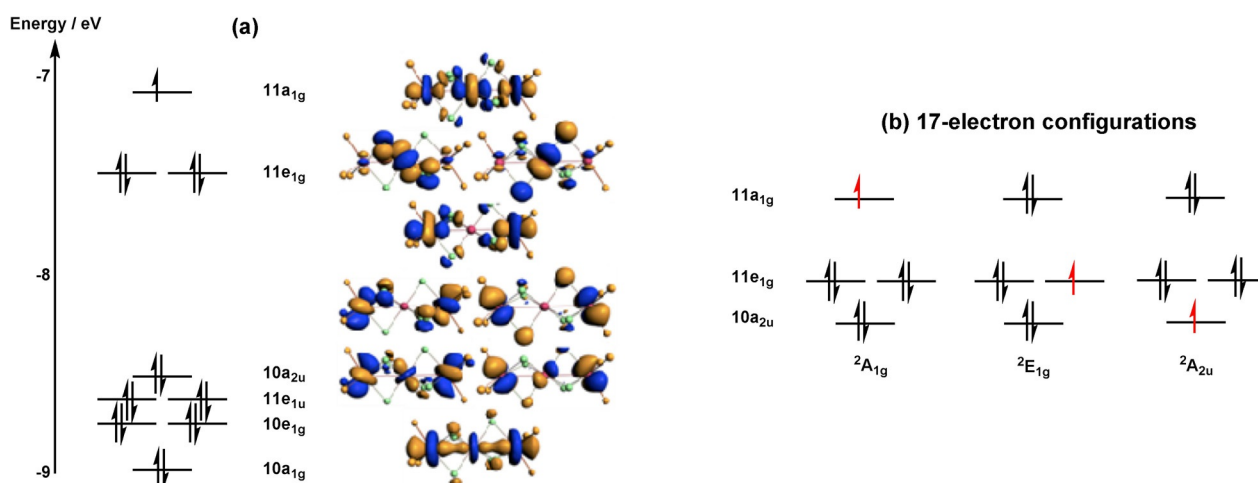
Figure 3. (a) Orbital array for the $^2A_{1g}$ ground state of 17-electron $[(PH_3)_3Ru(Cl)_3Ru(Cl)_3Ru(PH_3)_3]^{1+}$, $\mathbf{1'^{1+}}$ (b) Alternative configurations for a17-electron count.

16-Electron systems: The manifold of configurations available for the 16-electron system, shown in Figure 4 (top), is much richer due to the presence of two vacancies. These configurations can be grouped into three categories, depending on the location of the two vacant orbitals. In the first category, 1^1A_{1g}, 2^1A_{1g}, and $^3A_{2u}$, both vacancies reside in orbitals of local σ symmetry ($\sigma^2\delta_\pi^8$). In the second, the $^3E_{1g}$ and $^3E_{1u}$ configurations have one vacancy in the σ manifold and one in δ_π ($\sigma^3\delta_\pi^7$) while in the remaining configurations, both vacancies are located in the δ_π manifold ($\sigma^4\delta_\pi^6$). In anticipation of the discussion of the CASSCF wavefunctions, we note that the pairs of configurations $1/2^1A_{1g}$, $1/2^3E_{1g}$, $1/2^3E_{1u}$, and $1/2^3A_{2g}$ are all related by 2-electron excitations, and so may interact strongly in the configuration interaction (CI) matrix. We begin, however, with a discussion of the energies of the single configurations computed with DFT: relative energies are collected in Table 3 (lower), along with optimized structural parameters and Mulliken spin densities. For the all-ruthenium species $\mathbf{1'^{2+}}$, the ground state configuration at the B3LYP level is 1^1A_{1g}, precisely analogous to the $[Ru_3Cl_{12}]^{4-}$ system discussed by Bursten and Cotton.[12] With the BLYP functional, however, a very different picture emerges: the ground state is 1^3E_{1g} (albeit only 0.05 eV below 1^1A_{1g}) with a longer Ru—Ru bond of 3.12 Å caused by the single occupation of the $11a_{1g}$ orbital. The reversal of the stabilities of the 1^1A_{1g} and 1^3E_{1g} states highlights a general pattern wherein the B3LYP functional appears to systematically favor configurations with fewer electrons in the σ manifold ($10a_{2u}$, $11a_{1g}$) and more in δ_π ($11e_{1u}$, $11e_{1g}$). Whatever the origins of this trend, it is undeniably troubling that two popular functionals, BLYP and B3LYP, offer up such different pictures of the ground-state electronic structure.

A parallel study of the isoelectronic RuRhRu system, $\mathbf{2'^{3+}}$, presents a rather contrasting picture of the bonding, the most striking difference being that the 1^1A_{1g} state is now subject to a singlet instability which leads to spontaneous symmetry breaking and a more stable biradical state, BS($\sigma\sigma$) in Table 3. The closed-shell $^1A_{1g}$ and BS($\sigma\sigma$) states define the two limits of a continuous potential energy surface mapping the homolytic

fission of the metal-metal bonds, the so-called "Coulson–Fischer point" marking the point where the spin-restricted and spin-unrestricted curves diverge. Thus whilst the minimum for $\mathbf{1'^{2+}}$ lies to the left of the Coulson–Fischer point and has a closed-shell singlet ground state, the minimum for isoelectronic $\mathbf{2'^{3+}}$ lies to the right, with an open-shell singlet ground state. The tendency of the hybrid functional to favor configurations with vacancies in the σ manifold rather than δ_π is again apparent, and again it leads to different predictions of the ground state: $^3A_{2g}$ (zero vacancies in σ) for BLYP but $^3A_{2u}$ (two vacancies in σ) for B3LYP. The inclusion of Hartree–Fock exchange also magnifies the singlet instability, and the biradical state lies 0.88 eV below its closed-shell analogue. The broken-symmetry state and its ferromagnetic counterpart, the $^3A_{2u}$ state, lie within 0.02 eV for both functionals. The DFT study therefore presents a rather confused picture of the metal-metal bonding in these two isoelectronic systems: there is a clear shift towards weaker metal-metal bonding in the RuRhRu system, magnified in the case of the BLYP functional by the tendency to fill the orbitals of σ* symmetry. The identity of the ground state, and with it the qualitative description of metal-metal bonding, therefore depends critically on the choice of functional. In such circumstances, it is difficult to be confident that the apparent differences between the homo- and heterometallic chains are real, and not an artifact of the chosen methodology.

We have anticipated above that the presence of two different configurations of the same symmetry related by 2-electron excitations raises the possibility of strong multi-configurational character in the wavefunction. Moreover, these effects are likely to become increasingly significant as the metal-metal bonding becomes weaker, bringing the two configurations closer to degeneracy. To explore this possibility, we have turned to the Complete Active Space (CASSCF/PT2) ansatz for an alternative perspective. For both 16-electron systems, $\mathbf{1'^{2+}}$ and $\mathbf{2'^{3+}}$, we adopt a (10,6) active space that includes the six uppermost orbitals in Figure 3 ($10a_{2u}$, $11e_{1u}$, $11e_{1g}$, and $11a_{1g}$) and the ten valence electrons distributed amongst them. The active orbitals of $\mathbf{1'^{2+}}$ are shown in Figure 4. Attempts to
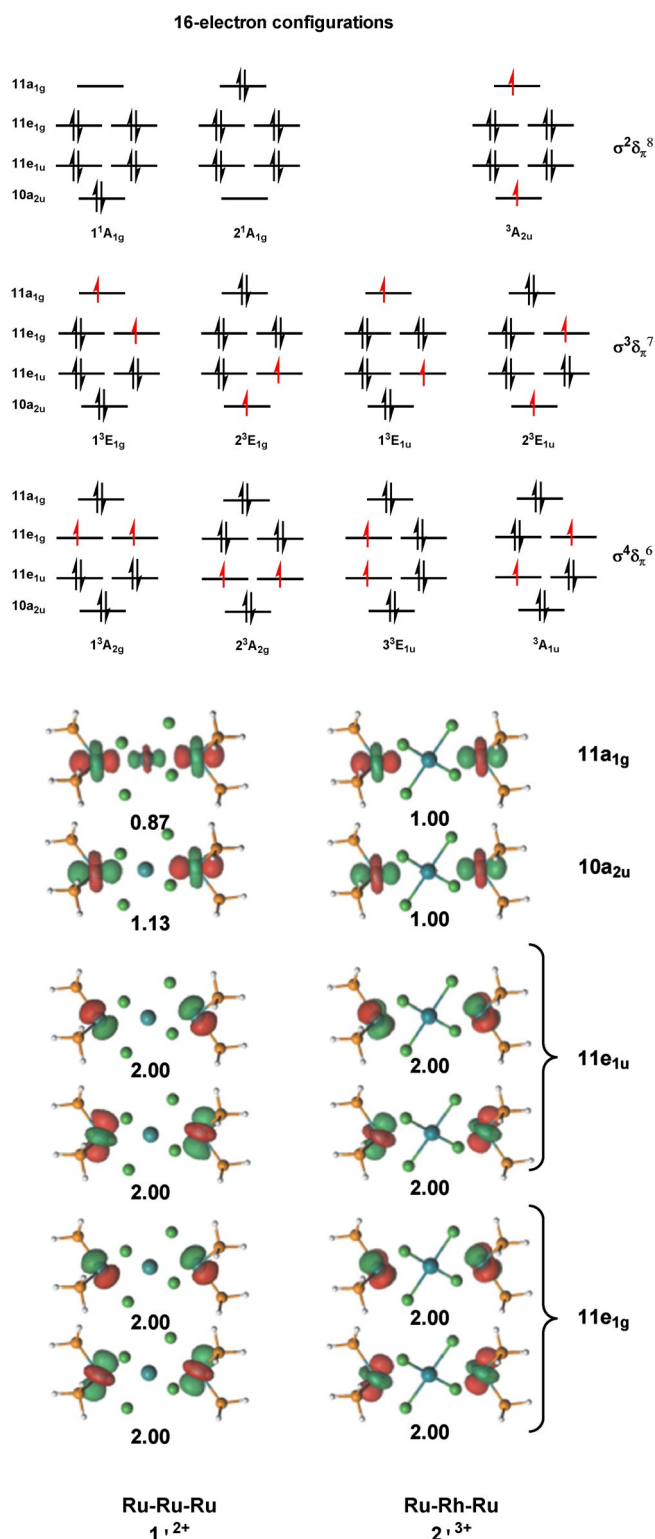
Figure 4. (a) Configurations available to the 16-electron system in a (10,6) active space and (b) Orbitals of the (10,6) active space and their occupations for the $^1A_{1g}$ states of $\mathbf{1}'^{2+}$ and $\mathbf{2}'^{3+}$.

this (10,6) active space yielded nine low-lying states, over which the orbitals were averaged. A detailed discussion of the active space and the identity of these nine low-lying states is given in the Supporting Information. Using the B3LYP-optimized geometry (Ru–Ru = 2.87 Å), the CASSCF wavefunction for the $^1A_{1g}$ ground state of $\mathbf{1}'^{2+}$ has contributions from both 1^1A_{1g} and 2^1A_{1g} configurations shown in Figure 4 with relative weights 0.56 and 0.44, giving overall occupations of 1.13 and 0.87 for the $10a_{2u}$ and $11a_{1g}$ orbitals, respectively. The substantial multi-configurational character is typical of relatively weak metal-metal bonds. At the same geometry, the $^3A_{2u}$ state, which is dominated by the single configuration of this symmetry in Figure 4 ($10a_{2u}^1 11a_{1g}^1$) lies 0.16 eV higher. States of $^3E_{1g}$ and $^3E_{1u}$ symmetry are at $+0.39$ and $+0.46$ eV, respectively, and both are extremely multi-configurational, as is the $^3A_{2g}$ state at $+0.99$. In light of the extreme multi-configurational character of the $^1A_{1g}$, $^3E_{1g}$, $^3E_{1u}$, and $^3A_{2g}$ states in the CASSCF wavefunction, it is clear that the DFT-computed energies of the single configurations shown in Table 3 must be treated with some caution. Indeed of those shown, only $^3A_{2u}$ and the broken-symmetry state can reasonably be represented by a single-determinant.

The corresponding (10,6) CASSCF wavefunction for $\mathbf{2}'^{3+}$ (at the B3LYP-optimized geometry of the diradical state with Ru-Rh = 3.09 Å) is qualitatively similar to that of $\mathbf{1}'^{2+}$. However, the $^3A_{2u}$ $^3E_{1g}$, $^3E_{1u}$, and $^3A_{2g}$ states now all lie within ≈ 0.1 eV of the $^1A_{1g}$ ground state, which is even more multi-configurational than in $\mathbf{1}'^{2+}$: the weights of the 1^1A_{1g} and 2^1A_{1g} configurations are identical at 0.50, giving equal occupations of 1.00 for both the $10a_{2u}$ and $11a_{1g}$ orbitals. We can link the more multi-configurational nature of the $^1A_{1g}$ CASSCF wavefunction to the emergence of a singlet instability in the closed-shell singlet at the DFT level: the localization of opposite-spin electrons in the biradical state mimics the effects of multi-configurational character by mixing singlet and triplet states. The comparison of $\mathbf{1}'^{2+}$ versus $\mathbf{2}'^{3+}$ at the CASCF/CASPT2 levels of theory therefore indicates a smooth transition from a covalently bonded scenario (albeit weak) to a classically exchange-coupled one.

Conclusion

In this paper we have reported the synthesis, structures and spectroelectrochemical properties of two new trimetallic chain compounds, $[(PEt_3)_3RuCl_3RhCl_3Ru(PEt_3)_3](CF_3SO_3)$ (**2**) and $[(PEt_3)_3RuCl_3IrCl_3Ru(PEt_3)_3]$ (**3**), isostructural with the all-ruthenium analogue, $[(PEt_3)_3RuCl_3RuCl_3Ru(PEt_3)_3]^+$, $\mathbf{1}^{1+}$. The replacement of an open-shell Ru^{III} cation (d^5) in the central position of the chain with a diamagnetic Rh^{III} unit (d^6) has a significant impact on the electronic structure. At the 17-electron level ($\mathbf{1}^{1+}$, $\mathbf{2/3}^{2+}$), the Rh^{III} or Ir^{III} unit substantially weakens the metal-metal bonding, an effect that is apparent in the DFT-computed electronic structure and also in the observed UV/Vis spectra. Differences are even more striking at the 16-electron level, but the identity of the ground state proves to be highly dependent on the choice of exchange correlation functional, making it difficult to establish a clear picture using DFT. The CASSCF wavefunction provides a more nuanced perspective,

expand this to a (16,9) active space that includes the six remaining electrons in $10e_{1g}$ and $10a_{1g}$ provided no further stabilization, and the occupations of the three additional orbitals remained close to 2.0. For both the singlet and triplet manifolds,

showing that the homo- and heterometallic systems differ only in the degree of multi-configurational character in the $^1A_{1g}$ ground state. The continuous variation in the composition of this wavefunction maps a transition from weak covalent 3-center-4-electron bonding in $\mathbf{1}^{2+}$ to an exchange-coupled scenario in $\mathbf{2}^{3+}$, where the Rh^{III} ion acts as a diamagnetic bridge between two paramagnetic Ru^{III} centers. This family of isostructural compounds highlights the axiom that covalent bonding and antiferromagnetic coupling are simply two ends of a continuum and it is, in principle, possible to design systems that lie between the two classical limits.

Experimental Section

Synthetic methods: [(PEt$_3$)$_3$RuCl$_3$RuCl$_3$Ru(PEt$_3$)$_3$](CF$_3$SO$_3$) (**1**) was prepared by the addition of a solution of [Ru(H$_2$O)$_3$(PEt$_3$)](CF$_3$SO$_3$)$_2$ (78 mg in 10ml of a 1:1 CH$_2$Cl$_2$/ethanol mixture, 0.096 mmol) to a CH$_2$Cl$_2$ solution of (Bu$_4$N)$_2$[RuCl$_6$] (36 mg in 10 mL, 0.045 mmol). The solution was stirred for 20 minutes before filtering. Evaporation to low volume under a stream of dinitrogen, followed by addition of diethyl ether to the resulting precipitate yielded the product, which was washed with water, ethanol, and finally ether. The air-dried crystalline compound was dissolved in minimal CH$_2$Cl$_2$/ethanol (7:1) and diethyl ether was added until the solution went cloudy. The mixture was then allowed to crystallize at $-20\,^{\circ}$C overnight. The green crystalline product was filtered, washed with diethyl ether, and dried at 70 °C at 0.01 mmHg. FABMS (MNBA) $m/z=$ 1225.6 ([(PEt$_3$)$_3$RuCl$_3$RuCl$_3$Ru(PEt$_3$)$_3$], 40 %); 1106.5 ([(PEt$_3$)$_3$RuCl$_3$RuCl$_3$Ru(PEt$_3$)$_2$], 20 %); 491.1 [ClRu(PEt$_3$)$_3$], 100 %); 371.1 ClRu(PEt$_3$)$_2$], 80 %); elemental analysis calcd (%) for C$_{37}$H$_{90}$Cl$_6$F$_3$O$_3$P$_6$Ru$_3$S: C 32.35, H 6.60; found: C 32.30, H 6.64.

[(PEt$_3$)$_3$RuCl$_3$RhCl$_3$Ru(PEt$_3$)$_3$](CF$_3$SO$_3$) (**2**) and [(PEt$_3$)$_3$RuCl$_3$RhCl$_3$Ru(PEt$_3$)$_3$](CF$_3$SO$_3$) (**3**) were prepared using the same procedure outlined above, except that (Bu$_4$N)$_2$[RhCl$_6$] or (Bu$_4$N)$_2$[IrCl$_6$] were used instead of (Bu$_4$N)$_2$[RuCl$_6$]. ^{1}H NMR (CD$_2$Cl$_2$): $\delta=1.88$ (m), 1.20 ppm (m); FABMS (MNBA) $m/z=1226.6$ ([(PEt$_3$)$_3$RuCl$_3$RhCl$_3$Ru(PEt$_3$)$_3$], 30 %); 1108.5 ([(PEt$_3$)$_3$RuCl$_3$RhCl$_3$Ru(PEt$_3$)$_2$], 15 %); 491.1 [ClRu(PEt$_3$)$_3$], 100 %); 371.1 ClRu(PEt$_3$)$_2$], 55 %); elemental analysis calcd for **2** C$_{37}$H$_{90}$Cl$_6$F$_3$O$_3$P$_6$RhRu$_2$S: C 32.20, H, 6.59; found: C 32.57, H 6.49; ^{1}H NMR (CD$_2$Cl$_2$): $\delta=1.88$ (m), 1.20 ppm (m); ^{31}P{^{1}H} NMR (CD$_2$Cl$_2$): $\delta=43.1$ ppm (s); FABMS (MNBA) $m/z=1316.6$ ([(PEt$_3$)$_3$RuCl$_3$IrCl$_3$Ru(PEt$_3$)$_3$], 55 %); 1198.6 ([(PEt$_3$)$_3$RuCl$_3$IrCl$_3$Ru(PEt$_3$)$_2$], 25 %); 491.1 [ClRu(PEt$_3$)$_3$], 100 %); 371.1 ClRu(PEt$_3$)$_2$], 85 %); elemental analysis calcd for **3** C$_{37}$H$_{90}$Cl$_6$F$_3$O$_3$P$_6$IrRu$_2$S: C 30.33, H 6.19, Cl 14.52; found: C 30.26, H 6.21, Cl 14.38.

Electrochemistry and spectroelectrochemistry: All electrochemical measurements were performed on chilled CH$_2$Cl$_2$ solutions, normally at 213 K, using a PAR 170 electrochemistry system; typical scan rates were 100 mV s^{-1} for cyclic voltammetry and 10 mV s^{-1} for alternating current voltammetry. The latter were recorded with positive feedback resistance compensation and phase-sensitive detection ($\omega=205$ Hz). Electrolyte solutions contained 0.5 mol dm^{-3} [NnBu$_4$][BF$_4$] and ca. 10^{-3} mol dm^{-3} of the complex. The solutions were purged and maintained under an atmosphere of N$_2$. The jacketed 10 cm^3 glass cell was fitted with a platinum-disc working electrode (0.5 mm diameter), platinum auxiliary electrode, Ag/AgCl reference electrode (against which ferrocene is oxidized at $+0.55$ V) isolated by a fritted salt bridge, and a submerged digital thermometer probe. An electronically controlled Lauda RL6 cryostat bath, circulating dry chilled MeOH, was used to maintain the low tem-

perature. Electronic spectra (45 000–3125 cm^{-1} that is, 222–3200 nm) were recorded with a Cary 5 near-IR to UV/Vis spectrophotometer. Spectra of oxidized species were obtained at 213 K by electro-generation at a Pt gauze electrode within a cryostatted optical semi-thin-layer electrochemical cell (path length 0.5 mm) mounted within the sample compartment of the spectrophotometer. Solutions contained 0.5 mol dm^{-3} [NnBu$_4$][BF$_4$] in CH$_2$Cl$_2$. The electro-generation potential was set ca. 200 mV beyond $E_{1/2}$ for each complex. Trustworthy results require strict isosbestic points and full recovery of the starting spectrum.

X-ray crystallography. The structures reported here rely on data collected in the year 2000 and solved, refined, and archived at that time. The structure of **2** is unmodified from the archived original. The structure of **3** has been refined using a slightly modified strategy closer to current practice. Data were collected on a KappaCCD diffractometer using graphite-monochromated Mo$_{K\alpha_1}$ radiation. Standard data collection and reduction procedures of the time were employed (see Supporting Information and CIFs therein for full details of structure determination and model refinement).[24]

Crystallographic data: C$_{36}$H$_{90}$Cl$_6$P$_6$RhRu$_2$·CF$_3$O$_3$S·CHCl$_3$, orthorhombic, $Pbnb$, $a=10.6290(2)$, $b=18.0160(2)$, $c=31.9420(4)$ Å, $V=6116.64(8)$ Å^3, $Z=4$, $T=200$ K, $\lambda=0.71073$ Å. 82 591 reflections, 6996 independent [$R_{(int)}=0.065$], $R1=0.039$, $wR2=0.041$ for 232 parameters and 4000 reflections $I>3\sigma(I)$ used in refinement. Max./Min. residual electron densities 0.87 and -0.64 e Å^{-3}. C$_{36}$H$_{90}$Cl$_6$IrP$_6$Ru$_2$·CF$_3$O$_3$S·2CHCl$_3$, triclinic, $P\bar{1}$, $a=9.93010(10)$, $b=10.7497(2)$, $c=15.9693(2)$ Å, $\alpha=77.8077(8)$, $\beta=81.8118(10)$, $\gamma=89.9327(8)^{\circ}$, $V=1648.48(4)$ Å^3, $Z=1$, $T=200$ K, $\lambda=0.71073$ Å. 51 597 measured reflections, 9662 independent [$R_{(int)}=0.057$]. $R1=0.041$, $wR2=0.045$ for 323 parameters and 7311 reflections $I>3\sigma(I)$. Max./Min. residual electron densities 2.39 and -2.36 e Å^{-3}. Technical aspects of the crystallography are summarized in Table 4, and bond lengths and angles for the cationic components of **2** and **3** are listed in Supporting Information, Table S1.

CCDC 1812829 (**2**) and 1812828 (**3**) contain the supplementary crystallographic data for this paper. These data are provided free of charge by The Cambridge Crystallographic Data Centre.

Computational methods: All DFT calculations in this paper were done with the Amsterdam Density Functional package (ADF2016.105).[25–27] Two functionals were used in this work, the gradient-corrected BLYP functional of Becke, Lee, Yang, and Parr[28,29] and its hybrid B3LYP,[30,31] in both cases with relativistic scalar corrections (ZORA). Triple-ζ Slater-type basis sets extended with a single polarization function (TZP) were used to describe the transition metals while double-ζ Slater-type basis sets extended with a single polarization function (DZP) was used for the main-group atoms. The frozen core approximation was used to treat the electrons in orbitals up to and including 4d on Ir, 3d on Rh and Ru, 2p on P and Cl, and 1s on C. For calculations with PMe$_3$ ligands, Grimme's corrections for dispersion were adopted.[32] Symmetry breaking was allowed by reducing the overall symmetry from D_{3d} to C_{3v} and polarizing the starting potential such that an excess of spin-α and spin-β density was placed on opposite ruthenium centers (ADF key "Modifystartpotential"). It should be emphasized that this allows the electrons to localize in a biradical state if this is more stable than the delocalized alternative, but it does not force them to do so: a spin polarized initial guess can always converge on the delocalized solution if this is more stable. The gradient algorithm of Versluis and Ziegler was used to optimize all structures.[33] Time-dependent DFT was used to calculate UV/Visible spectra.[34] Single point CASSCF/CASPT2 calculations were done by using the MOLCAS 8.0 package.[35] The orbitals expanded by applying the atomic natural orbitals optimized for relativistic corrections

Table 4. Crystallographic data for $[(PEt_3)_3RuCl_3RhCl_3Ru(PEt_3)_3](CF_3SO_3)$ (**2**) and $[(PEt_3)_3RuCl_3IrCl_3Ru(PEt_3)_3](CF_3SO_3)$ (**3**).

	2	3
space group	*Pbnb*	*P1̄*
a [Å]	10.6287(2)	9.93010(10)
b [Å]	18.0157(2)	10.7497(2)
c [Å]	31.9420(4)	15.9693(2)
α [°]	90	77.8077(8)
β [°]	90	81.8118(10)
γ [°]	90	89.9327(8)
V [Å^3]	6116.4(2)	1648.48(4)
T [K]	200	200
λ [Å]	0.71073	0.71073
Z	4	1
ρ_{calcd} [Mg m^{-3}]	1.426	1.716
μ [mm^{-1}]	1.38	3.17
R_1	0.039	0.041
wR_2	0.041	0.045

and core correlation (ANO-RCC) basis sets.[36] The large primitive set of functions is contracted to [7s6p4d2f1g] for Rh and Ru, [4s3p1d] for P and Cl, and [1s] for H. In both systems, the orbitals were averaged over the lowest nine states of each multiplicity (singlets and triplets). The reasons for averaging over nine states are discussed in Supporting Information. The Cholesky decomposition with threshold of 1.0 e^{-8} was used for the two-electron integrals.[37]

Acknowledgements

Conflict of interest

The authors declare no conflict of interest.

Keywords: CASSCF · density functional theory · metal—metal bonds · spectroelectrochemistry · tri-metallic

[1] J. E. McGrady in "*Molecular Metal-Metal Bonds*" (Ed.: S. T Liddle), Wiley-VCH, Weinheim, **2015**.

[2] U. Kölle, J. Kossakowski, N. Klaff, L. Wesemann, U. Englert, G. E. Heberich, *Angew. Chem. Int. Ed. Engl.* **1991**, *30*, 690 – 691; *Angew. Chem.* **1991**, *103*, 732 – 733.

[3] R. H. Summerville, R. Hoffmann, *J. Am. Chem. Soc.* **1979**, *101*, 3821 – 3831.

[4] a) T. Lovell, J. E. McGrady, R. Stranger, S. A. Macgregor, *Inorg. Chem.* **1996**, *35*, 3079 – 3080; b) J. E. McGrady, R. Stranger, T. Lovell, *Inorg. Chem.* **1997**, *36*, 3242; c) R. Poli, H. D. Mui, *Inorg. Chem.* **1991**, *30*, 65 – 77.

[5] K. Saito, Y. Nakao, H. Sato, S. Sakaki, *J. Phys. Chem. A* **2006**, *110*, 9710 – 9717.

[6] A. Bino, F. A. Cotton, *J. Am. Chem. Soc.* **1980**, *102*, 608 – 611.

[7] J. C. Fettinger, J. C. Gordon, S. P. Mattamana, C. J. O'Connor, R. Poli, G. Salem, *Inorg. Chem.* **1996**, *35*, 7404 – 7412.

[8] W. H. Delphin, R. A. D. Wentworth, M. S. Matson, *Inorg. Chem.* **1974**, *13*, 2552 – 2555.

[9] L. Chen, F. A. Cotton, *Polyhedron* **1998**, *17*, 3727 – 3734.

[10] M. Schroeder, S. Hartwig, K. W. Krämer, S. Decurtins, H. Hillebrecht, *Inorg. Chem.* **2012**, *51*, 8385 – 8393.

[11] J. W. Hewage, G. Cavigliasso, R. Stranger, *Inorg. Chem.* **2015**, *54*, 10632 – 10641.

[12] B. E. Bursten, F. A. Cotton, A. Fang, *Inorg. Chem.* **1983**, *22*, 2127 – 2133.

[13] J. Darriet, *Rev. Chim. Min.* **1981**, *18*, 27 – 32.

[14] F. A. Cotton, M. Matusz, R. C. Torralba, *Inorg. Chem.* **1989**, *28*, 1516 – 1520.

[15] F. A. Cotton, R. C. Torralba, *Inorg. Chem.* **1991**, *30*, 3293 – 3304.

[16] F. A. Cotton, R. C. Torralba, *Inorg. Chem.* **1991**, *30*, 4386 – 4391.

[17] R. Goerissen, U. Kölle, T. P. Spaniol, *Polyhedron* **1992**, *11*, 2317 – 2320.

[18] a) J. E. McGrady, *Angew. Chem. Int. Ed.* **2000**, *39*, 3077 – 3079; *Angew. Chem.* **2000**, *112*, 3216 – 3219; b) V. Arcisauskaite, C. de Graaf, M. Spivak, J. E. McGrady, *Phys. Chem. Chem. Phys.* **2016**, *18*, 24006 – 24014; c) V. Arcisauskaite, M. Spivak, J. E. McGrady, *Inorg. Chim. Acta* **2015**, *424*, 293 – 299.

[19] G. A. Heath, K. A. Moock, D. W. A. Sharp, L. J. Yellowlees, *J. Chem. Soc. Chem. Commun.* **1985**, 1503 – 1505.

[20] B. D. Yeomans, D. G. Humphrey, G. A. Heath, *J. Chem. Soc. Dalton Trans.* **1997**, 4153 – 4166.

[21] F. Barrière, W. Geiger, *J. Am. Chem. Soc.* **2006**, *128*, 3980 – 3989.

[22] a) N. S. Hush, J. K. Beattie, V. M. Ellis, *Inorg. Chem.* **1984**, *23*, 3339 – 3342; b) R. S. Armstrong, W. A. Horsfield, K. W. Nugent, *Inorg. Chem.* **1990**, *29*, 4551 – 4556.

[23] B. J. Kennedy, G. A. Heath, T. J. Khoo, *Inorg. Chim. Acta* **1991**, *190*, 265 – 269.

[24] P. W. Betteridge, J. R. Carruthers, R. I. Cooper, K. Prout, D. J. Watkin, *J. Appl. Crystallogr.* **2003**, *36*, 1487.

[25] G. te Velde, F. M. Bickelhaupt, E. J. Baerends, C. Fonseca Guerra, S. J. A. van Gisbergen, J. G. Snijders, T. Ziegler, *J. Comput. Chem.* **2001**, *22*, 931 – 967.

[26] C. F. Guerra, J. G. Snijders, G. te Velde, E. J. Baerends, *Theor. Chem. Acc.* **1998**, *99*, 391 – 403.

[27] E. J. Baerends, T. Ziegler, A. J. Atkins, J. Autschbach, D. Bashford, O. Baseggio, A. Bérces, F. M. Bickelhaupt, C. Bo, P. M. Boerritger, L. Cavallo, C. Daul, D. P. Chong, D. V. Chulhai, L. Deng, R. M. Dickson, J. M. Dieterich, D. E. Ellis, M. van Faassen, L. Fan, T. H. Fischer, C. Fonseca Guerra, M. Franchini, A. Ghysels, A. Giammona, S. J. A. van Gisbergen, A. Goez, A. W. Götz, J. A. Groeneveld, O. V. Gritsenko, M. Grüning, S. Gusarov, F. E. Harris, P. van den Hoek, Z. Hu, C. R. Jacob, H. Jacobsen, L. Jensen, L. Joubert, J. W. Kaminski, G. van Kessel, C. König, F. Kootstra, A. Kovalenko, M. V. Krykunov, E. van Lenthe, D. A. McCormack, A. Michalak, M. Mitoraj, S. M. Morton, J. Neugebauer, V. P. Nicu, L. Noodleman, V. P. Osinga, S. Patchkovskii, M. Pavanello, C. A. Peeples, P. H. T. Philipsen, D. Post, C. C. Pye, H. Ramanantoanina, P. Ramos, W. Ravenek, J. I. Rodríguez, P. Ros, R. Rüger, P. R. T. Schipper, D. Schlüns, H. van Schoot, G. Schreckenbach, J. S. Seldenthuis, M. Seth, J. G. Snijders, M. Solà, M. Stener, M. Swart, D. Swerhone, V. Tognetti, G. te Velde, P. Vernooijs, L. Versluis, L. Visscher, O. Visser, F. Wang, T. A. Wesolowski, E. M. van Wezenbeek, G. Wiesenekker, S. K. Wolff, T. K. Woo, A. L. Yakovlev, ADF2017, SCM, Theoretical Chemistry, Vrije Universiteit, Amsterdam, The Netherlands, https://www.scm.com.

[28] A. D. Becke, *Phys. Rev. A* **1988**, *38*, 3098 – 3100.

[29] C. Lee, W. Yang, R. G. Parr, *Phys. Rev. B* **1988**, *37*, 785 – 789.

[30] A. D. Becke, *J. Chem. Phys.* **1993**, *98*, 5648 – 5652.

[31] P. J. Stephens, F. J. Devlin, C. F. Chabalowski, M. J. Frisch, *J. Phys. Chem.* **1994**, *98*, 11623 – 11627.

[32] S. Grimme, S. Ehrlich, L. Goerigk, *J. Comput. Chem.* **2011**, *32*, 1457 – 1465.

[33] L. Versluis, T. Ziegler, *J. Chem. Phys.* **1988**, *88*, 322 – 328.

[34] S. J. A. van Gisbergen, J. G. Snijders, E. J. Baerends, *Comput. Phys. Commun.* **1999**, *118*, 119 – 138.

[35] F. Aquilante, J. Autschbach, R. K. Carlson, L. F. Chibotaru, M. G. Delcey, L. De Vico, I. F. Galván, N. Ferré, L. M. Frutos, L. Gagliardi, M. Garavelli, A. Giussani, C. E. Hoyer, G. Li Manni, H. Lischka, D. X. Ma, P. A. Malmqvist, T. Müller, A. Nenov, M. Olivucci, T. B. Pedersen, D. L. Peng, F. Plasser, B.

Pritchard, M. Reiher, I. Rivalta, I. Schapiro, J. Segarra-Marti, M. Stenrup, D. G. Truhlar, L. Ungur, A. Valentini, S. Vancoillie, V. Veryazov, V. P. Vysotskiy, O. Weingart, F. Zapata, R. Lindh, *J. Comput. Chem.* **2016**, *37*, 506–541.

[36] B. O. Roos, V. Veryazov, P. O. Widmark, *Theor. Chem. Acc.* **2003**, *111*, 345–351.

[37] F. Aquilante, P.-Å. Malmqvist, T. B. Pedersen, A. Ghosh, B. O. Roos, *J. Chem. Theory Comput.* **2008**, *4*, 694–702.